

The Effect of the Slit Configuration on the H₂ 1-0 S(1) to Br γ Line Ratio of Spatially Resolved Planetary Nebulae

Isabel Aleman¹★

¹UNIFEI, Instituto de Física e Química, Universidade Federal de Itajubá, Av. BPS 1303 Pinheirinho, 37500-903 Itajubá, MG, Brazil

Accepted XXX. Received YYY; in original form ZZZ

ABSTRACT

The H₂ 1-0 S(1)/Br γ ratio ($R(\text{Br}\gamma)$) is used in many studies of the molecular content in planetary nebulae (PNe). As these lines are produced in different regions, the slit configuration used in spectroscopic observations may have an important effect on their ratio. In this work, observations and numerical simulations are used to demonstrate and quantify such effect in PNe. The study aims to assist the interpretation of observations and their comparison to models. The analysis shows that observed $R(\text{Br}\gamma)$ ratios reach only values up to 0.3 when the slit encompasses the entire nebula. Values higher than that are only obtained when the slit covers a limited region around the H₂ peak emission and the Br γ emission is then minimised. The numerical simulations presented show that, when the effect of the slit configuration is taken into account, photoionization models can reproduce the whole range of observed $R(\text{Br}\gamma)$ in PNe, as well as the behaviour described above. The argument that shocks are needed to explain the higher values of $R(\text{Br}\gamma)$ is thus not valid. Therefore, this ratio is not a good indicator of the H₂ excitation mechanism as suggested in the literature.

Key words: planetary nebulae: general – circumstellar matter – astrochemistry – ISM: molecules – photodissociation region (PDR)

1 INTRODUCTION

As the most abundant molecular species in planetary nebulae (PNe), the emission of H₂ is of great interest. Molecular hydrogen lines have been detected in the near infrared (IR) spectrum of more than 130 planetary nebulae (PNe) (e.g., Treffers et al. 1976; Isaacman 1984; Kastner et al. 1996; Lumsden et al. 2001; Guerrero et al. 2000; Davis et al. 2003; Likkell et al. 2006; Ramos-Larios et al. 2017; Gledhill et al. 2018, see also Appendix A). Kastner et al. (1996) found a H₂ detection rate of 40 per cent. Recent deep imaging detections of H₂ in small structures in PNe indicate that this rate may be even higher (Fang et al. 2018; Akras et al. 2017, 2020a).

Most of the published H₂ spectroscopic observations of PNe uses narrow slits or small apertures¹ including only part of the planetary nebula (see Table A1). Sometimes only extractions of the slit observation are considered. Often the authors focus on specific positions in the nebula, for example, obtaining a spectrum with a slit centred at the H₂ 1-0 S(1) line emission peak.

The position and width of the slit aperture during a observation have a great impact on the measured line fluxes and derived line ratios demonstrated by Fernandes et al. (2005), Gesicki et al. (2016), and Akras et al. (2020b) studies for optical atomic lines. Fernandes et al. (2005), for example, studied the effects of the nebular area covered by the slit on the atomic line ratios and derived quantities in H II regions. Their results showed that ratios of low to high-ionization lines are sensitive to this area. The ratios of [O II], [N II] and [S II] optical lines to H β can be affected by up to 30% in relation to the ratio of the entire ionized nebula. The difference of the emitting regions of each of the lines (low-ionization lines are emitted in the outer layers of the nebula) is responsible for such high percentage. The effect of the slit configuration on atomic line ratios can be important when studying diagnostic diagrams or comparing observations to models as showed by Akras et al. (2020b).

It is therefore expected that the effect of the slit aperture and position can also be important for the H₂ line ratios to Br γ as they are not produced in the same region. The H₂ 1-0 S(1)/Br γ ratio (hereafter $R(\text{Br}\gamma)$) has been used in several studies of the molecular content of PNe, as proxies of the H₂ quantity (Aleman & Gruenwald 2004, 2011) and assisting the diagnostic of the acting excitation mechanisms (Marquez-Lugo et al. 2015).

This paper studies the effect of the slit configuration on

★ E-mail: bebel.aleman@gmail.com

¹ To simplify the text, only slit observations will be mentioned, but most of the discussion also applies or can be easily extended to observations with different shape apertures.

the $R(\text{Bry})$ ratio, using observations available in the literature and numerical simulations to verify and quantify such effect. The observations used here are described in Sect. 2 and a table is given in Appendix A. The numerical simulations are described in Sect. 3. The results of the analysis of the slit configuration effect is presented in Section 4. Conclusions are summarised in Sect. 5.

2 OBSERVATIONS

For the present work, H_2 and Bry line fluxes and ratios from observations were compiled from the literature. The data collected is presented in Table A1 (see Appendix A). The table shows the $R(\text{Bry})$ line ratios obtained from spectroscopic observations of PNe and information on the corresponding slit configuration. The table also includes a few other relevant characteristics of the PNe, which are used in the present analysis.

The slit centred at the nebular centre and positioned across the entire nebula (indicated as “centred” in Fig. 1) is the most typical PN observation configuration used for optical nebular analysis, i.e., for works focused on the ionized region. Although also used in studies of the H_2 component in extended objects, other common position in this case is the narrow slit positioned at the H_2 emission peak (indicated as “ H_2 peak” in Fig 1). Observing the *whole nebula* is only possible for more compact and/or distant PNe. In Table 1, the observations are classified within four general slit configurations as follows:

- *Centred*: the slit is positioned across the whole nebula passing by its centre;
- *H_2 peak*: centred at the H_2 1-0 S(1) emission peak;
- *Whole nebula*: when the slit encompass the entire nebula;
- *Other*: all other configurations that do not falls under the previous categories or the configuration is not clear from the paper description.

This nomenclature will be used hereafter to indicate the slit positions for both observations and simulations.

In Fig. 1, the illustration shows a round nebula, but the above classification is extended for all PNe morphologies. Bipolar PNe observations considered as *centred* are those with the slit across the equatorial region, perpendicular to the symmetry axis. In bipolar PNe, the waist region is usually a bright structure in H_2 emission (Kastner et al. 1996). This region shows a torus or barrel-like structure. For the purposes of this paper, what is of importance is the hydrogen species that are sampled by the slit (this will become clear further in the text.). It is then not difficult to see that using the slit across this torus/barrel is analogous to the *centred* position for elliptical PNe, despite the angle the bipolar is observed. For bipolar PNe, observations considered as *H_2 peak* are those where the slit samples a limited region around the wall of the torus, the wall of the lobes, or any known H_2 bright position.

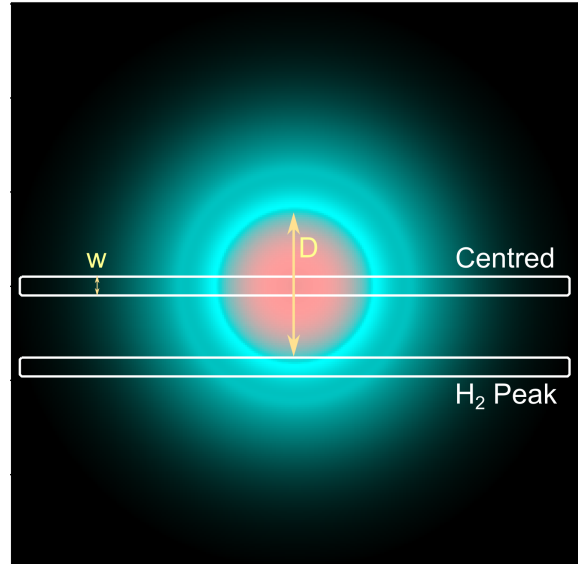


Figure 1. Simulated image of a spherical PN in the Bry, H_2 1-0 S(1), and H_2 2-1 S(1) line emission, represented by red, green, and blue colours, respectively. The simulation uses the parameters of the reference model listed in Table 1. The two rectangles indicate the slit positions *centred* and *H_2 peak*. D is the diameter of the PN and w is the slit width.

3 SIMULATIONS

To simulate the slit observations of the nebula, we use the Python² library PYCLOUDY (version 0.9.6; Morisset 2013). PYCLOUDY provides pseudo-3D simulations from CLOUDY one-dimensional models outputs. The library produces simulated line emission maps, which allow the simulation of slit observations in any configuration and the calculation of the corresponding line fluxes.

Numerical calculations of the H_2 and Bry emissivity in PNe were obtained with the photoionization code CLOUDY (version 17.01; Ferland et al. 2017). CLOUDY can simulate a photoionized nebula from the ionized to the neutral regions (photodissociation region, PDR) self-consistently. As shown in Aleman & Gruenwald (2004, 2011) and Aleman et al. (2011), this is very important for the calculation of the H_2 infrared emission, in special for the PNe with high-temperature central stars.

In the present models, the ionizing source emits as a blackbody, here described by its effective temperature (T_{eff}) and bolometric luminosity (L_{\star}). The gas is assumed to be spherically distributed. Models were calculated for two gas density (n_{H}) distributions: (i) uniform density and (ii) diffuse gas with a denser surrounding shell. For the first case, we studied density values from $n_{\text{H}} = 10^3$ to 10^5 cm^{-3} . In the second case, the diffuse gas is assumed to have $n_{\text{H}} = 10^3 \text{ cm}^{-3}$ and the shell $n_{\text{H}} = 10^5 \text{ cm}^{-3}$. Shell models were simulated with different central star temperatures and shell distances from the central star. For each set of central star parameters, simulations with four different shell distances were studied. The position were set where $\text{H}^0/\text{H} = 10^{-4}$, 10^{-3} , 10^{-2} , and 5×10^{-1} . All simulations are done

² <http://www.python.org>

Table 1. Reference Model Parameters.

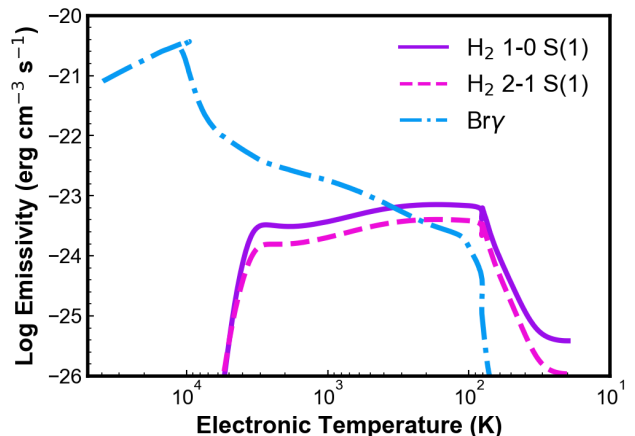
Component	Parameter	Value
Central Star:	Temperature	100 000 K
	Luminosity	$3\,000 L_{\odot}$
Gas:	n_H	$1\,000\text{ cm}^{-3}$
	Abundances	Solar (Grevesse et al. 2010)
Dust:	Material	Graphite
	Distribution	CLOUDY ISM (Mathis et al. 1977)
	Dust-to-Gas Ratio	3×10^{-3}

with solar abundance (Grevesse et al. 2010). Although different abundance sets may change the atomic line fluxes and therefore the gas cooling rates, such differences will not affect the conclusions of this paper. Dust is included in the models uniformly mixed with the gas. Aleman & Gruenwald (2004) showed that the dust composition in the regular dust model included in photoionization codes is not a significant factor for the H_2 emission (due to the similarities in the general behaviour of their opacities). On the other hand, dust size and density may greatly influence the H_2 emission (Aleman & Gruenwald 2011). Here, Cloudy models with graphite dust and dust grain size distribution typical for the ISM were explored. Dust-to-gas ratios of 3×10^{-2} and 3×10^{-3} were studied (Stasińska & Szczerba 1999). All the models were calculated assuming a 2 kpc distance, but this value has no effect on the present results, as they are based on distance-independent quantities.

For convenience, reference values are defined in Table 1. Unless stated otherwise the model parameters are the reference values listed in that table.

The present models simulate the physical conditions and emissivities along the PN radial outward direction from an inner radius of 10^{15} cm to a distance to the central star where the gas temperature decreases to $T_F = 40$ K. This value was chosen based on inspection of the H_2 emissivity radial profiles calculated with Cloudy and to reproduce well the observations. Such stop criterion guarantee the inclusion of most of the H_2 ro-vibrational lines 1-0 S(1) and 2-1 S(1) emitting region. Figure 2 provides an example of behaviour of the emissivities of such H_2 lines and Bry as a function of the gas temperature.

Different stopping temperatures were tested. For $T_F > 100$ K (cut the nebula closer to the central star), a significant portion of the total nebular H_2 emission would have been ignored (unless the cloud is limited by matter). For models with $T_F = 100$ K, more than 70 % of the flux determined for the model with $T_F = 40$ K would have been ignored. For $T_F = 60$ K, the flux ignored is approximately 50-70 %. On the other hand, extending the nebula for very low T_F , could produce an unrealistic large PN and the low line emissivity in such regions would not contribute much to the flux. For temperatures lower than 40 K, the H_2 1-0 S(1) and 2-1 S(1) line emissivities decreases and affects very little the total calculated flux (Fig. 2). The difference in the fluxes found for $T_F = 40$ K and $T_F = 20$ K is less than a factor of two, which will not affect our conclusions.

**Figure 2.** Line emissivities as a function of the gas temperature for the reference model with parameters given in Table 1. The gas temperature axis is shown in inverted order so the distance to the central star increases to the right.

The observation simulations were performed with PY-CLOUDY, using a slit placed in two positions, *centred* and *H₂ peak*, as discussed in the previous section. Fig. 1 shows the configurations. The two slit apertures (white boxes) are positioned over a simulated PNe (reference model). The slit length is longer than the nebula size. For both cases, we study simulations where the slit width w is varied from a small fraction of the nebula diameter up to a size that includes the whole nebula. The *whole nebula* configuration can therefore be understood as a special limit case of both of the configurations above, when the slit width is large enough to cover the entire nebula.

4 RESULTS

4.1 The Effect of the Slit Configuration

As the H_2 1-0 S(1) and Bry lines are produced in different regions in the nebula (Fig. 2) the effect of the slit configuration on the $R(\text{Bry})$ ratio in spatially-resolved observations can be significant. Indeed, Figure 3 demonstrates that both the slit configuration and the fraction of the nebula covered by the slit can have a large influence in the $R(\text{Bry})$ values.

Figure 3 shows $R(\text{Bry})$ as a function of the w/D ratio, i.e., ratio of the slit width (w) to the diameter of the PN ionized region (D). The ionized region diameter D is used for convenience, as it is more commonly available than the total PN size (including the neutral region). When this value is not found, other diameter is used. The value will be of similar order and as this only happens for a small fraction for the sample, it will not affect the results of this work. For bipolar PNe, D is assumed to be the width taken in the minor axis of the object. As H_2 is more often seen in the torus/waist region or the wall of the lobes in bipolar PNe, the minor axis size would then be a better analogous dimension to D of spherical PNe. The plot in Fig. 3 includes all the data collected from the literature listed in Table A1. The lower values of $R(\text{Bry})$ are limited for the observation sensitivity. This is what causes the empty lower left area in Fig. 3.

There is a clear segregation of $R(\text{Bry})$ values in Fig. 3

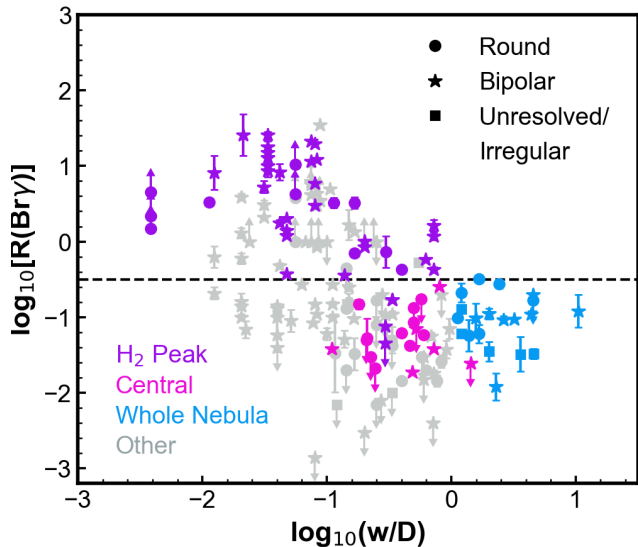


Figure 3. $R(\text{Bry})$ as a function of the ratio of the slit width (w) to the diameter of the PN ionized region (D). Measurements are taken with configurations H_2 peak (violet), centred (pink), whole nebula (cyan) and others (grey). The morphology of the object is indicated by the different symbols: dots for round, stars for bipolar and multipolar, squares for irregular and unresolved PNe. Error bars are shown when uncertainties are available. Upper and down arrows indicate lower and upper limits, respectively. The black dashed line indicates the maximum value found for whole nebula measurements.

related to the slit configuration. The ratios obtained in the *centred* and *whole nebula* configurations show a similar range of values. In these cases, there is no indication of significant trends $R(\text{Bry})$ w/D . The maximum value found for $R(\text{Bry})$ is 0.3 (indicated by the dashed line in the figure).

The H_2 peak and *other* configurations exhibit the largest line ratios, which can be up to three orders of magnitude larger than the ratios measured for the *whole nebula* or using the *centred* configuration. For H_2 peak, most observations are found with $R(\text{Bry}) > 0.3$.

There is also a trend for higher $R(\text{Bry})$ values being found towards small w/D . For H_2 peak observations, such trend can be naturally understood in terms of the different regions emitting H_2 and Bry lines and the different regions covered by the slit in each configuration. For a given nebula, D is fixed, so decreasing w/D , corresponds to using narrower slits. As w decreases, the region around the H_2 peak will include less Bry emission, maximising the ratio $R(\text{Bry})$ (see Figs. 1 and 2). In the case of *other* configuration, a similar behaviour might be occurring.

For the bipolar PNe observations, a classification scheme analogue to the scheme for round objects was used. Observations considered as *centred* are those with the slit across the equatorial region, perpendicular to the symmetry axis. The torus is usually a bright structure in H_2 emission in bipolar PNe (Kastner et al. 1996). Observations considered as H_2 peak were taken with the slit sampling the wall of the torus, the wall of the lobes or at any known H_2 bright position. The results found, i.e. segregation and values, are the same as found for the round PNe.

4.2 Simulations of $R(\text{Bry})$ for Different Slit Configurations

The study of models presented in this section has two goals: (i) to test our interpretation of the effect showed in the previous Section and (ii) to test if general photoionization models can reproduce the observed range of $R(\text{Bry})$ values if the slit configuration is taken into account. The second goal is of interest, as it is sometimes argued that UV excitation simulations cannot reproduce the observed values of $R(\text{Bry})$ in PNe (e.g., Marquez-Lugo et al. 2015). Comparison of observed with modelled H_2 emission in PNe are done using zero- or one-dimensional models in many published works (e.g., Vicini et al. 1999; Lumsden et al. 2001; Kelly & Hrivnak 2005; Aleman & Gruenwald 2011; Marquez-Lugo et al. 2015; Akras et al. 2020a), but in most of them the slit configuration during the observation is not taken into account in the comparison.

Figure 4 shows simulations of the $R(\text{Bry})$ ratio for round, uniform density PNe. Each panel shows two PN models calculated for a given T_{eff} and with two different dust-to-gas ratios; the other parameters are from the reference model (Table 1). For each PN model, three curves are generated: the cyan horizontal line indicates the values of $R(\text{Bry})$ calculated from fluxes integrated in the *whole nebula*; the pink and the purple curves show the ratios calculated using the *centre* and H_2 peak configurations, respectively, as a function of w/D . The colour code used for the models is thus the same as used for the observations in Fig. 3.

Observations of PNe with a similar temperature (within ± 10 kK) are included in each of the plots for comparison. Even with the simplicity of these models, the calculated values can represent reasonably well the general behaviour and, in most cases, the magnitude of the observed $R(\text{Bry})$.

For low w/D , ratios for the *centre* position are smaller than for those obtained with the *whole nebula* configuration. The difference is less than one order of magnitude. On the other hand, for the H_2 peak configuration, smaller values of w/D produce larger values of $R(\text{Bry})$, as the slit will be covering progressively less ionized emission, without varying much the molecular emission. A plateau is reached in progressively lower w/D for increasing T_{eff} . As seen in Fig 2, even in the neutral region, there is a vestigial H ionization degree. For both configurations, when w/D gets larger than one (slit covering most to all the nebula) the values tend to the *whole nebula* value, as should be expected.

For two objects, BD+30°3639 and Hubble 12 (Hb 12), there are a number of observations with different configurations published. For these two objects, there are observations using the all the configurations we discuss previously. The observations are shown individually in the plots of Fig. 5. The models from Fig 4 with $T_{\text{eff}} = 50$ kK, which is close to the object's T_{eff} , are also included. The models presented in this section were not developed to fit specific objects. No attempt to match specific characteristics of the object (apart for the close T_{eff}) was done. As mentioned above, these are simplified models. The goal here is only another sanity check, by verifying that the general behaviour and magnitude of the observed effect for individual objects are also reasonably reproduced by the models.

Models with different PN parameters, within typical ranges (see Aleman & Gruenwald 2011, and references

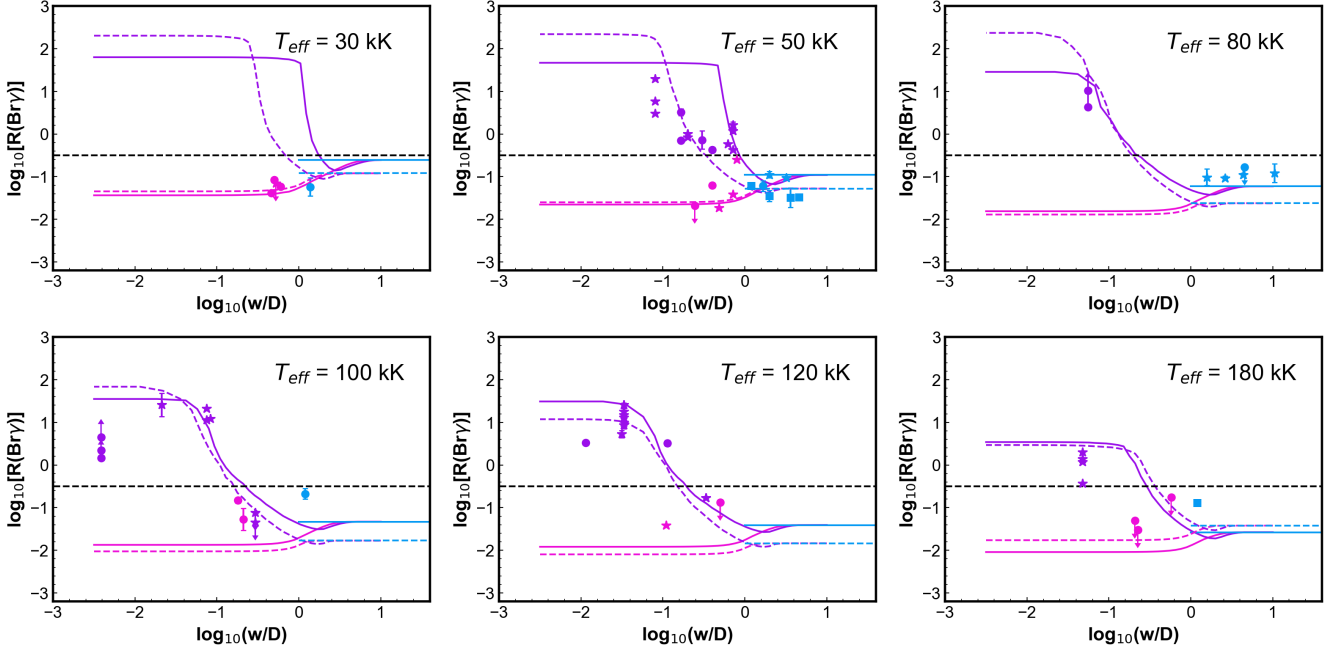


Figure 4. Ratio $R(Br\gamma)$ as a function of the ratio w/D . Curves in each panel represent uniform density model with the T_{eff} indicated. Solid curves uses dust-to-gas ratio of 3×10^{-3} and dashed curves 3×10^{-2} . Dots are observations of PNe with a similar temperature (± 10 kK). The colour code indicates the slit position as in Fig 3. The black dashed line indicates the upper value found for the *whole nebula* configuration.

therein) were also studied. In Fig. 4, the differences in $R(Br\gamma)$ due the central star temperature and dust-to-gas ratio are shown. The general behaviour of the curves is similar for different star luminosities, within a typical PNe range. Changing the model luminosity in one order of magnitude for more or less change the curves in a similar amount as the change in dust-to-gas ratio shown. Variation in density within typical PNe values (10^3 - 10^5 cm^{-3}) may account for the differences between observations and models in *whole nebula* and *centre* configurations. However, models with high densities ($>10^5$ cm^{-3}) produces large differences between the H_2 *peak* $R(Br\gamma)$ calculated and observed. This is natural, as dense models produce very compact nebulae, while the H_2 *peak* observations usually probe sub-structures in more extended PNe, likely more diffuse nebulae.

Molecular hydrogen emission is often associated with dense clumpy shells or torus structures (Kastner et al. 1996; Matsuura et al. 2007; Marquez-Lugo et al. 2015; Akras et al. 2017). For this reason, simulations were also made for PNe models where a diffuse gas is surrounded by a dense shell, as describe in Sect. 3. In Fig. 6, results are shown for shells placed at different distances from the central star. Results are analogous to those from Fig. 4. They also reproduce the observations qualitatively and quantitatively. The comparison with observations shows improvement in the match of observations and models with relation to the uniform density models, especially for *centre* and *whole nebula* ratios.

Models with shell internal radius at $H^0/H = 10^{-4}$ (solid thin) represents well most *whole nebula* and *centre* observations. On the other hand, models with shell at $H^0/H = 10^{-3}$, 10^{-2} , and 5×10^{-1} , reproduces well most of the H_2 *peak* observations, as well as some of the other configurations. This may be reflecting the ionization structures being probed by

the observations. The H_2 *peak* configuration probes structures farther from the central star, while *whole nebula* and *centre* is likely to have a stronger influence of the more ionized emission.

The simulations presented here shows that simple photoionization models can reproduce the general behaviour with w/D and the range of observed values if they consider the slit configuration.

4.3 On $R(Br\gamma)$ as an H_2 Excitation Mechanism Diagnostic

Marquez-Lugo et al. (2015) proposed the diagram $R(H_2)$ vs. $R(Br\gamma)$ to analyse the excitation mechanism of H_2 . Figure 7 shows this diagram for the data in Table A1. In the top plot, all observations with both ratios available are shown with error bars when available. The loose positive correlation seen by Marquez-Lugo et al. (2015) is also observed here. In the plot, there is indication of two different populations, which become clear in the middle panel, where the observations are separated according to the slit configuration. The segregation in the $R(Br\gamma)$ values for different configurations seen in Fig. 3 is also seen in the diagram. Observations including the *whole nebula* and with the slit *centred* exhibit only $R(Br\gamma)$ values smaller than 0.3, as previously shown. Values $R(Br\gamma) > 0.3$ are obtained by H_2 *peak* observations or *other* configurations. For both H_2 *peak* and *whole nebula*, a positive correlation between $R(H_2)$ and $R(Br\gamma)$ is seen. No conclusion can be made for *centre* observations, as there are only a few points. All configurations show a similar range of $R(H_2)$, which indicates that both H_2 lines are produced in the same or very similar regions, as shown in Fig 2.

The bottom plot in Fig. 7 shows that the H_2 *peak* points

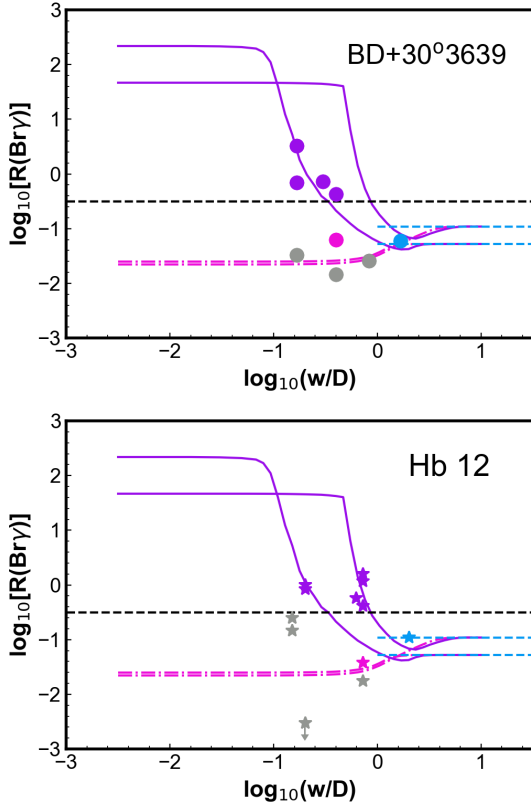


Figure 5. Plots as in Fig. 4, where models included are for $T_{eff} = 50$ kK and observations are for the ring PN BD+30°3639 in the top panel and for the bipolar PN Hb 12 in the bottom panel (in this panel error bars are not include as they, when available, are smaller than the marker size).

with both $R(H_2)$ and $R(Bry)$ high values are observed with less nebular area cover by the slit (lower w/D). From their diagram, [Marquez-Lugo et al. \(2015\)](#) conclude that shock excitation is the dominant mechanism when $R(H_2) > 1$. They based their conclusion in two arguments: (i) the thermalisation of the H_2 emission of such objects (when $R(H_2) \sim 10$) and (ii), in their words, “that shock-excitation (...) is a much more efficient excitation mechanism than UV fluorescence and thus produces higher levels of emission in the H_2 lines”. However, according to the results shown here, taking into consideration the slit position in the photoionization simulations such values can easily be reached. This is not an argument against shock excitation, which cannot be discard, but the results presented here show that the observations with higher $R(Bry)$ are biased by the slit effect and argument (ii) above is not valid. If photoprocesses dominate the H_2 excitation, high density gas could explain the high values $R(H_2)$ usually attributed to shocks. Models by [Sternberg & Dalgarno \(1989\)](#) showed that UV excitation (not only shocks) may thermalize the H_2 level population for sufficiently high optical depths (see also discussions in [Hora & Latter 1994](#); [Akras et al. 2020a](#)). [Marquez-Lugo et al. \(2015\)](#) suggested to separate UV excitation from shocks do not necessary follows.

5 CONCLUSIONS

This paper presented the analysis of the slit configuration effect on the $R(Bry)$ ratio in PNe, using observations and numerical simulations. The main results are:

- The H_2 1-0 S(1) and Bry lines are produced in different regions in the nebula, and, therefore, the slit configuration used in the spectroscopic observations strongly affects the $R(Bry)$ ratio.
- For round and ring-like PNe, $R(Bry)$ ratios obtained with a slit across the entire nebula passing by its centre (*centred*) provides similar values to those obtained by integrating the line flux over the *whole nebula*. Similar result is obtained for bipolar PNe when observing with the slit across the equatorial region, perpendicular to the main nebular axis (also considered here *centred*).
- The $R(Bry)$ ratios derived from observations in the *centred* configuration or when the *whole nebula* is integrated reach only values up to 0.3. Values higher than this are only obtained when the slit is positioned at the H_2 *peak* positions.
- The $R(Bry)$ ratio measured with the slit at the H_2 *peak* emission depends on the fraction of the nebula covered by the slit. The largest values of $R(Bry)$ are found when the slit covers a small fraction of the nebula.
- When the slit configuration is taken into account, the simple photoionization models presented here can represent very well the range of values and the general behaviour of the observed $R(Bry)$.
- The result above shows that the argument that shocks are needed to explain the higher values of $R(Bry)$ is not valid. Therefore, this ratio is not a good indicator of the H_2 excitation mechanism as suggested by [Marquez-Lugo et al. \(2015\)](#).
- All the results showed here demonstrate the importance of considering the slit configuration in studies involving the $R(Bry)$ ratio.

It is important to notice that analogous results could be obtained for shock models if they produce similar H_2 and Bry emission distribution. It is not the aim of this work to defend photoprocesses over shocks as the dominant H_2 excitation mechanism in PNe. Here the focus is on geometrical effects and the intention is just to bring the attention to the effect of the slit configuration.

ACKNOWLEDGEMENTS

This study was financed in part by the Coordenação de Aperfeiçoamento de Pessoal de Nível Superior - Brasil (CAPES) - Finance Code 001. The author is thankful to S. Akas and H. Monteiro for useful discussions and their suggestions to improve this manuscript. This research has made use of the NASA’s Astrophysics Data System and the SIMBAD database, operated at CDS, Strasbourg, France ([Wenger et al. 2000](#)). This work has also made use of the computing facilities available at the Laboratory of Computational Astrophysics of the Universidade Federal de Itajubá (LAC-UNIFEI). The LAC-UNIFEI is maintained with grants from CAPES, CNPq and FAPEMIG.

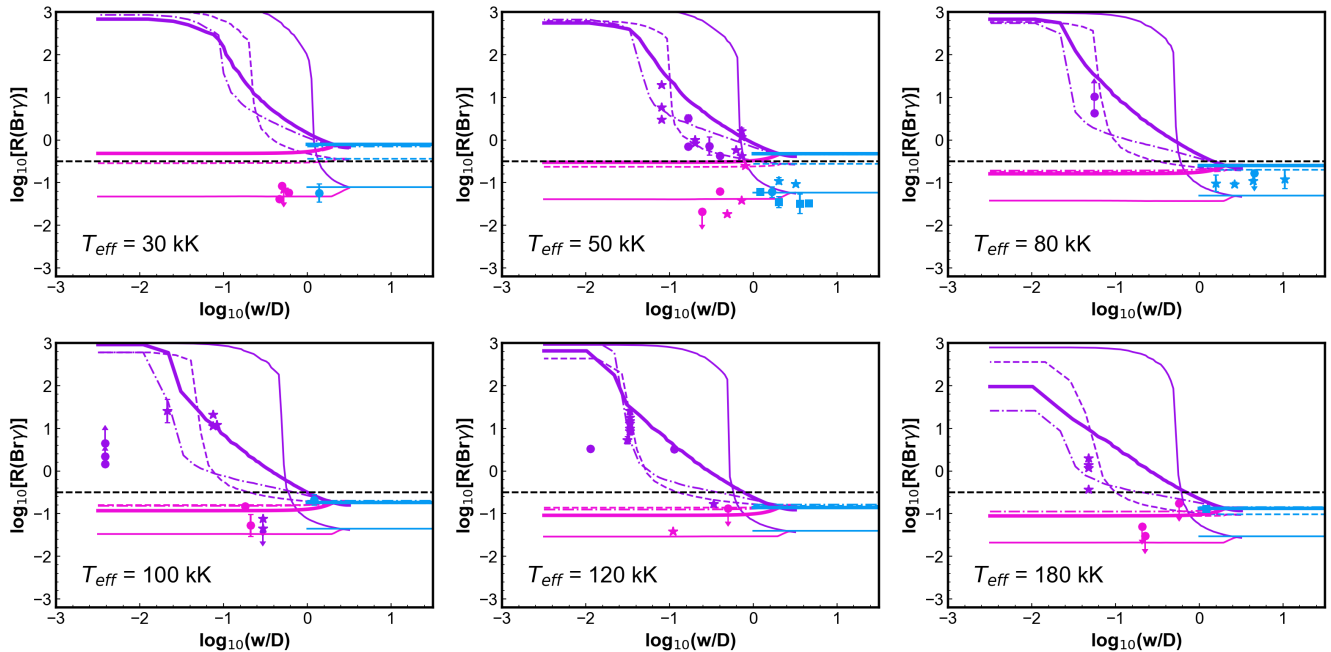


Figure 6. Ratio $R(Bry)$ as a function of the ratio w/D . Curves in each panel represent shell models with the T_{eff} indicated and the parameters as in Table 1. Curves are presented for models with shells simulated at ionization degree of $H^0/H = 10^{-4}$ (solid thin), 10^{-3} (dashed), 10^{-2} (dot-dashed), and 5×10^{-1} (solid thick). Dots are observations of PNe with a similar temperature (within 10 kK). The colour code is the same as in Fig 3. The black dashed line indicates the upper value found for the *whole nebula* configuration.

DATA AVAILABILITY

The data underlying this article are available in the article. Any additional information can be request to the Author.

REFERENCES

- Akras S., Boumis P., Meaburn J., Alikakos J., López J. A., Gonçalves D. R., 2015, *MNRAS*, **452**, 2911
- Akras S., Gonçalves D. R., Ramos-Larios G., 2017, *MNRAS*, **465**, 1289
- Akras S., Gonçalves D. R., Ramos-Larios G., Aleman I., 2020a, *MNRAS*,
- Akras S., Monteiro H., Aleman I., Farias M. A. F., May D., Pereira C. B., 2020b, *MNRAS*, **493**, 2238
- Aleman I., Gruenwald R., 2004, *ApJ*, **607**, 865
- Aleman I., Gruenwald R., 2011, *A&A*, **528**, A74
- Aleman I., Zijlstra A. A., Matsuura M., Gruenwald R., Kimura R. K., 2011, *MNRAS*, **416**, 790
- Banerjee D. P. K., Anandarao B. G., 1991, *A&A*, **250**, 165
- Barría D., Kimeswenger S., 2018, *MNRAS*, **480**, 1626
- Bear E., Soker N., 2017, *ApJ*, **837**, L10
- Beckwith S., Persson S. E., Gatley I., 1978, *ApJ*, **219**, L33
- Christianto H., Seaquist E. R., 1998, *AJ*, **115**, 2466
- Clyne N., Redman M. P., Lloyd M., Matsuura M., Singh N., Meaburn J., 2014, *A&A*, **569**, A50
- Cuesta L., Phillips J. P., 2000, *ApJ*, **543**, 754
- Davis C. J., Smith M. D., Stern L., Kerr T. H., Chiar J. E., 2003, *MNRAS*, **344**, 262
- De Marco O., Crowther P. A., Barlow M. J., Clayton G. C., de Koter A., 2001, *MNRAS*, **328**, 527
- Dinerstein H. L., Lester D. F., Carr J. S., Harvey P. M., 1988, *ApJ*, **327**, L27
- Fang X., Guerrero M. A., Miranda L. F., Riera A., Velázquez P. F., Raga A. C., 2015, *MNRAS*, **452**, 2445

- Fang X., Zhang Y., Kwok S., Hsia C.-H., Chau W., Ramos-Larios G., Guerrero M. A., 2018, *ApJ*, **859**, 92
- Feibelman W. A., 1997, *ApJS*, **109**, 481
- Ferland G. J., et al., 2017, *Rev. Mex. Astron. Astrofis.*, **53**, 385
- Fernandes I. F., Gruenwald R., Viegas S. M., 2005, *MNRAS*, **364**, 674
- Frew D. J., 2008, PhD thesis, Department of Physics, Macquarie University, NSW 2109, Australia
- García-Hernández D. A., Manchado A., García-Lario P., Domínguez-Tagle C., Conway G. M., Prada F., 2002, *A&A*, **387**, 955
- Geballe T. R., Burton M. G., Isaacman R., 1991, *MNRAS*, **253**, 75
- Gesicki K., Zijlstra A. A., Morisset C., 2016, *A&A*, **585**, A69
- Gledhill T. M., Froebrich D., Campbell-White J., Jones A. M., 2018, *MNRAS*, **479**, 3759
- Grevesse N., Asplund M., Sauval A. J., Scott P., 2010, *Ap&SS*, **328**, 179
- Guerrero M. A., Miranda L. F., 2012, *A&A*, **539**, A47
- Guerrero M. A., Villaver E., Manchado A., Garcia-Lario P., Prada F., 2000, *ApJS*, **127**, 125
- Harrington J. P., Lane N. J., White S. M., Borkowski K. J., 1997, *AJ*, **113**, 2147
- Heap S. R., Hintzen P., 1990, *ApJ*, **353**, 200
- Henry R. B. C., Kwitter K. B., Dufour R. J., 1999, *ApJ*, **517**, 782
- Herald J. E., Bianchi L., 2004, *ApJ*, **611**, 294
- Hora J. L., Latter W. B., 1994, *ApJ*, **437**, 281
- Hora J. L., Latter W. B., Deutsch L. K., 1999, *ApJS*, **124**, 195
- Hsia C.-H., Chau W., Zhang Y., Kwok S., 2014, *ApJ*, **787**, 25
- Hua C. T., 1988, *A&A*, **193**, 273
- Hyung S., Aller L. H., Feibelman W. A., Lee W.-B., 2001, *AJ*, **122**, 954
- Isaacman R., 1984, *A&A*, **130**, 151
- Kaler J. B., Jacoby G. H., 1989, *ApJ*, **345**, 871
- Kastner J. H., Weintraub D. A., Gatley I., Merrill K. M., Probst R. G., 1996, *ApJ*, **462**, 777

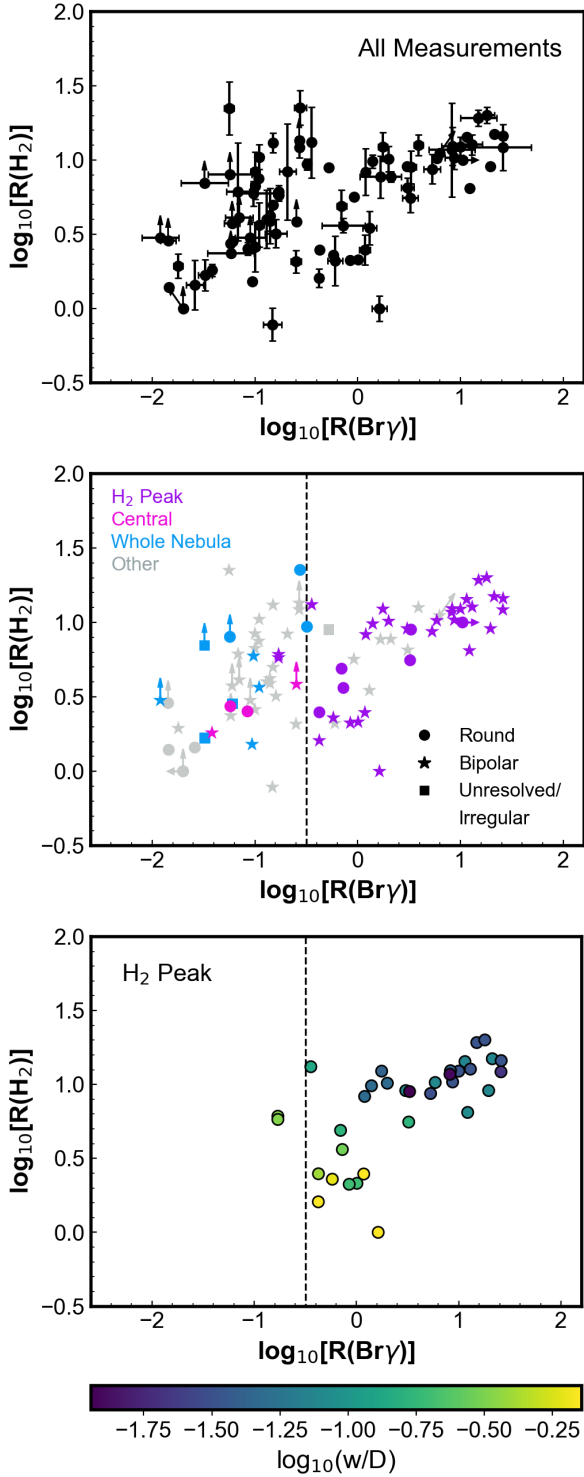


Figure 7. Diagnostic diagram proposed by [Marquez-Lugo et al. \(2015\)](#). Observations shown are from Table A1. *Top*: All measurements showing error bars when uncertainties are available. Down/up arrows associated with symbols indicate upper/lower limits. *Middle*: All measurements classified by slit configuration and object morphology. Error bars are omitted for clarity. *Bottom*: Only the H_2 peak observations are shown. The dot colour code indicates the parameter $\log_{10}(w/D)$. Observations with small w/D occupy the region where [Marquez-Lugo et al. \(2015\)](#) attribute to shocks. The black dashed line indicates the upper value found for $R(\text{Br}\gamma)$ in the *whole nebula* configuration.

- Kelly D. M., Hrivnak B. J., 2005, *ApJ*, **629**, 1040
 Kwok S., Chong S.-N., Hsia C.-H., Zhang Y., Koning N., 2010, *ApJ*, **708**, 93
 Latter W. B., Dayal A., Bieging J. H., Meakin C., Hora J. L., Kelly D. M., Tielens A. G. G. M., 2000, *ApJ*, **539**, 783
 Lau R. M., Werner M., Sahai R., Ressler M. E., 2016, *ApJ*, **833**, 115
 Leal-Ferreira M. L., Gonçalves D. R., Monteiro H., Richards J. W., 2011, *MNRAS*, **411**, 1395
 Likkell L., Dinerstein H. L., Lester D. F., Kindt A., Bartig K., 2006, *AJ*, **131**, 1515
 Lopez J. A., Falcon L. H., Ruiz M. T., Roth M., 1991, *A&A*, **241**, 526
 Lopez J. A., Tapia M., Roth M., 1993, in Weinberger R., Acker A., eds, IAU Symposium Vol. 155, Planetary Nebulae. p. 208
 Luhman K. L., Rieke G. H., 1996, *ApJ*, **461**, 298
 Lumsden S. L., Puxley P. J., Hoare M. G., 2001, *MNRAS*, **328**, 419
 Manchado A., Stanghellini L., Villaver E., García-Segura G., Shaw R. A., García-Hernández D. A., 2015, *ApJ*, **808**, 115
 Marquez-Lugo R. A., Guerrero M. A., Ramos-Larios G., Miranda L. F., 2015, *MNRAS*, **453**, 1888
 Marston A. P., Bryce M., Lopez J. A., Palmer J. W., Meaburn J., 1998, *A&A*, **329**, 683
 Mashburn A. L., Sterling N. C., Madonna S., Dinerstein H. L., Roederer I. U., Geballe T. R., 2016, *ApJ*, **831**, L3
 Mathis J. S., Rimpl W., Nordsieck K. H., 1977, *ApJ*, **217**, 425
 Matsuura M., et al., 2007, *MNRAS*, **382**, 1447
 Miller T. R., Henry R. B. C., Balick B., Kwitter K. B., Dufour R. J., Shaw R. A., Corradi R. L. M., 2019, *MNRAS*, **482**, 278
 Miranda L. F., Vázquez R., Torrelles J. M., Eiroa C., Lopez J. A., 1997, *MNRAS*, **288**, 777
 Miranda L. F., Vázquez R., Corradi R. L. M., Guerrero M. A., López J. A., Torrelles J. M., 1999, *ApJ*, **520**, 714
 Monteiro H., Morisset C., Gruenwald R., Viegas S. M., 2000, *ApJ*, **537**, 853
 Morisset C., 2013, pyCloudy: Tools to manage astronomical Cloudy photoionization code, Astrophysics Source Code Library (ascl:1304.020)
 O'Dell C. R., Ferland G. J., Henney W. J., Peimbert M., 2013, *AJ*, **145**, 92
 Otsuka M., Kemper F., Hyung S., Sargent B. A., Meixner M., Tajitsu A., Yanagisawa K., 2013, *ApJ*, **764**, 77
 Otsuka M., Parthasarathy M., Tajitsu A., Hubrig S., 2017, *ApJ*, **838**, 71
 Phillips J. P., 2003, *MNRAS*, **344**, 501
 Phillips J. P., Reay N. K., White G. J., 1983, *MNRAS*, **203**, 977
 Phillips J. P., White G. J., Harten R., 1985, *A&A*, **145**, 118
 Pottasch S. R., Bernard-Salas J., Roellig T. L., 2009a, *A&A*, **499**, 249
 Pottasch S. R., Surendiranath R., Bernard-Salas J., Roellig T. L., 2009b, *A&A*, **502**, 189
 Preite-Martinez A., Acker A., Koeppen J., Stenholm B., 1989, *A&AS*, **81**, 309
 Preite-Martinez A., Acker A., Koeppen J., Stenholm B., 1991, *A&AS*, **88**, 121
 Ramos-Larios G., Guerrero M. A., Miranda L. F., 2008, *AJ*, **135**, 1441
 Ramos-Larios G., Vázquez R., Guerrero M. A., Olguín L., Marquez-Lugo R. A., Bravo-Alfaro H., 2012, *MNRAS*, **423**, 3753
 Ramos-Larios G., Guerrero M. A., Sabin L., Santamaría E., 2017, *MNRAS*, **470**, 3707
 Ramsay S. K., Chrysostomou A., Geballe T. R., Brand P. W. J. L., Mountain M., 1993, *MNRAS*, **263**, 695
 Rudy R. J., Lynch D. K., Mazuk S., Puetter R. C., Dearborn D. S. P., 2001, *AJ*, **121**, 362
 Sahai R., Morris M. R., Villar G. G., 2011, *AJ*, **141**, 134

Shaw R. A., Stanghellini L., Villaver E., Mutchler M., 2006, *ApJS*, **167**, 201

Shupe D. L., Armus L., Matthews K., Soifer B. T., 1995, *AJ*, **109**, 1173

Smith H. A., Larson H. P., Fink U., 1981, *ApJ*, **244**, 835

Stanghellini L., Villaver E., Manchado A., Guerrero M. A., 2002, *ApJ*, **576**, 285

Stanghellini L., García-Lario P., García-Hernández D. A., Perea-Calderón J. V., Davies J. E., Manchado A., Villaver E., Shaw R. A., 2007, *ApJ*, **671**, 1669

Stanghellini L., Shaw R. A., Villaver E., 2008, *ApJ*, **689**, 194

Stanghellini L., Shaw R. A., Villaver E., 2016, *ApJ*, **830**, 33

Stasińska G., Szczerba R., 1999, *A&A*, **352**, 297

Sternberg A., Dalgarno A., 1989, *ApJ*, **338**, 197

Storey J. W. V., 1984, *MNRAS*, **206**, 521

Surendiranath R., Pottasch S. R., García-Lario P., 2004, *A&A*, **421**, 1051

Szyska C., Walsh J. R., Zijlstra A. A., Tsamis Y. G., 2009, *ApJ*, **707**, L32

Szyska C., Zijlstra A. A., Walsh J. R., 2011, *MNRAS*, **416**, 715

Treffers R. R., Fink U., Larson H. P., Gautier III T. N., 1976, *ApJ*, **209**, 793

Tylenda R., Siódmiak N., Górny S. K., Corradi R. L. M., Schwarz H. E., 2003, *A&A*, **405**, 627

Vázquez R., 2012, *ApJ*, **751**, 116

Vicini B., Natta A., Marconi A., Testi L., Hollenbach D., Draine B. T., 1999, *A&A*, **342**, 823

Walsh J. R., et al., 2018, *A&A*, **620**, A169

Webster B. L., Payne P. W., Storey J. W. V., Dopita M. A., 1988, *MNRAS*, **235**, 533

Wenger M., et al., 2000, *A&AS*, **143**, 9

Yuan H. B., Liu X. W., Péquignot D., Rubin R. H., Ercolano B., Zhang Y., 2011, *MNRAS*, **411**, 1035

APPENDIX A: VALUES AND REFERENCES OF THE H_2 OBSERVATIONS USED IN THE TEXT

Table A1 lists the H_2 observations from the literature used in this paper. Column 1 shows the name of the PN and the code for the position observed according to the authors of the original paper, cited in Column 10. Column 2 and 3 gives the stellar temperature and its reference, respectively. $R(H_2)$ and $R(Bry)$, with errors when available, are given in Columns 4 to 7. The slit width and position used in the H_2 observation are given in Columns 8 and 9, respectively. The PN morphological classification, the value assumed for its diameter, and their references are given in Column 11 to 13.

Most of the stellar temperature values are of Zanstra temperatures, with preference given for values inferred from He II lines. If effective temperatures are determined from direct star observations, preference is given for such value. If those are not available, then values determined from other methods are used.

The morphology listed in the table is a general classification based on the published literature cited in Table A1 (which is listed below). The objects with ring morphology in which a bipolar structure is not clear are considered here in the class of round nebulae. Whether such nebula is really round or torus-like (thus bipolar) will not affect the result given that the ionization structure is being taken in account during the current analysis.

References for the H_2 observations: Be78: Beckwith

et al. (1978), Da03: Davis et al. (2003), Di88: Dinerstein et al. (1988), DM01: De Marco et al. (2001), Ge91: Geballe et al. (1991), GH02: García-Hernández et al. (2002), HL94: Hora & Latter (1994), Ho99: Hora et al. (1999), Is84: Isaacman (1984), Li06: Likkell et al. (2006), LR96: Luhman & Rieke (1996), Lu01: Lumsden et al. (2001), Ma16: Mashburn et al. (2016), ML15: Marquez-Lugo et al. (2015), Ot13: Otsuka et al. (2013), Ph83: Phillips et al. (1983), Ph85: Phillips et al. (1985), Ra93: Ramsay et al. (1993), RL08: Ramos-Larios et al. (2008), Ru01: Rudy et al. (2001), Sm81: Smith et al. (1981), St84: Storey (1984), Vi99: Vicini et al. (1999), We88: Webster et al. (1988).

References for T_* : Fr08: Frew (2008), HH90: Heap & Hintzen (1990), Hu88: Hua (1988), KJ89: Kaler & Jacoby (1989), La00: Latter et al. (2000), Lu01: Lumsden et al. (2001), Ma15: Manchado et al. (2015), Ma16: Mashburn et al. (2016), Ot13: Otsuka et al. (2013), Ot17: Otsuka et al. (2017), Ph03: Phillips (2003), PM89: Preite-Martinez et al. (1989), PM91: Preite-Martinez et al. (1991), St02: Stanghellini et al. (2002), Sz09: Szyska et al. (2009).

References for D : Ak15: Akras et al. (2015), BA91: Banerjee & Anandarao (1991), BK18: Barría & Kimeswenger (2018), Be17: Bear & Soker (2017), Cl14: Clyne et al. (2014), CS98: Christiano & Seaquist (1998), CP00: Cuesta & Phillips (2000), Da03: Davis et al. (2003), DM01: De Marco et al. (2001), Fa15: Fang et al. (2015), Fa18: Fang et al. (2018), Fe97: Feibelman (1997), GH02: García-Hernández et al. (2002), GM12: Guerrero & Miranda (2012), Gu00: Guerrero et al. (2000), Ha97: Harrington et al. (1997), He99: Henry et al. (1999), HB04: Herald & Bianchi (2004), HL94: Hora & Latter (1994), Hs14: Hsia et al. (2014), Hy01: Hyung et al. (2001), Kw10: Kwok et al. (2010), La16: Lau et al. (2016), LF11: Leal-Ferreira et al. (2011), Li06: Likkell et al. (2006), Lo93: Lopez et al. (1993), Lo01: Lopez et al. (1991), ML15: Marquez-Lugo et al. (2015), Ma98: Marston et al. (1998), Mi18: Miller et al. (2019), Mi97: Miranda et al. (1997), Mi99: Miranda et al. (1999), Mo00: Monteiro et al. (2000), OD03: O'Dell et al. (2013), Ot13: Otsuka et al. (2013), Po09: Pottasch et al. (2009b), Po09b: Pottasch et al. (2009a), RL08: Ramos-Larios et al. (2008), RL12: Ramos-Larios et al. (2012), Sa11: Sahai et al. (2011), Sh06: Shaw et al. (2006), Sh95: Shupe et al. (1995), St07: Stanghellini et al. (2007), St08: Stanghellini et al. (2008), St16: Stanghellini et al. (2016), SS99: Stasińska & Szczerba (1999), St84: Storey (1984), Su04: Surendiranath et al. (2004), Sz11: Szyska et al. (2011), Ty03: Tylenda et al. (2003), Va12: Vázquez (2012), Vi99: Vicini et al. (1999), Wa18: Walsh et al. (2018), We88: Webster et al. (1988), Yu11: Yuan et al. (2011).

This paper has been typeset from a $\text{\TeX}/\text{\LaTeX}$ file prepared by the author.

Table A1. Observations Database

Object	T_{\star} (10^3 K)	T_{\star} Ref.	$R(H_2)$	$R(H_2)$ Error	$R(Bry)$	$R(Bry)$ Error	w (arcsec)	Slit Position	H_2 Ref.	Morph.	D (arcsec)	D Ref.
BD+30 ^o 3639	45.7	Ph03			0.060	0.017	10.0	Whole	Be78	R	6.0	Ha97
BD+30 ^o 3639	45.7	Ph03	1.4	0.6	0.026	0.005	5.0	Other	Ge91	R	6.0	Ha97
BD+30 ^o 3639 OE	45.7	Ph03	4.9	1.2	0.698	0.079	1.0	H ₂ Peak	Ho99	R	6.0	Ha97
BD+30 ^o 3639 N Ring	45.7	Ph03			0.033	0.016	1.0	Other	Ho99	R	6.0	Ha97
BD+30 ^o 3639 H ₂ Lobe	45.7	Ph03	5.6	1.2	3.238	0.569	1.0	H ₂ Peak	Ho99	R	6.0	Ha97
BD+30 ^o 3639 Core	45.7	Ph03	1.4		0.015		2.4	Other	Lu01	R	6.0	Ha97
BD+30 ^o 3639 Nebula	45.7	Ph03			0.062		2.4	Centre	Lu01	R	6.0	Ha97
BD+30 ^o 3639 H ₂ Zone	45.7	Ph03	2.5		0.424		2.4	H ₂ Peak	Lu01	R	6.0	Ha97
BD+30 ^o 3639 E	45.7	Ph03	3.6	0.4	0.726	0.351	1.8	H ₂ Peak	Li06	R	6.0	Ha97
Cn 3-1	53.6	Ph03			< 0.015		1.8	Other	Li06	B	3.0	Mi97
Hb 5	131.0	Ph03			< 0.200		5.0	Other	We88	B	18.0	Ty03
Hb 5 up	131.0	Ph03	13.1	2.0	0.1500	0.010	2.0	Other	Da03	B	18.0	Ty03
Hb 5 cen	131.0	Ph03	2.6	1.0	0.100	0.010	2.0	Other	Da03	B	18.0	Ty03
Hb 5 dn	131.0	Ph03	12.2	2.0	0.270	0.010	2.0	Other	Da03	B	18.0	Ty03
Hb 12	45.5	Ph03			0.111	0.019	10.0	Whole	Be78	B	5.0	ML15
Hb 12	45.5	Ph03	1.0	0.2	1.629	0.273	3.6	H ₂ Peak	Di88	B	5.0	ML15
Hb 12	45.5	Ph03	2.3	0.1	0.579	0.018	3.1	H ₂ Peak	Ra93	B	5.0	ML15
Hb 12 Core	45.5	Ph03			< 0.003		1.0	Other	HL96	B	5.0	ML15
Hb 12 3.7" E	45.5	Ph03	2.1		1.009		1.0	H ₂ Peak	HL96	B	5.0	ML15
Hb 12 3.7" E 2" S	45.5	Ph03	2.1		0.847		1.0	H ₂ Peak	HL96	B	5.0	ML15
Hb 12 central 1	45.5	Ph03	1.9	0.4	0.018	0.002	3.6	Other	LR96	B	5.0	ML15
Hb 12 central 2	45.5	Ph03	1.8	0.2	0.038	0.002	3.6	Centre	LR96	B	5.0	ML15
Hb 12 west	45.5	Ph03	2.5	0.6	1.175	0.142	3.6	H ₂ Peak	LR96	B	5.0	ML15
Hb 12 east	45.5	Ph03	1.6	0.2	0.423	0.033	3.6	H ₂ Peak	LR96	B	5.0	ML15
Hb 12 PA -5 ^o Ring	45.5	Ph03	0.8	0.2	0.148	0.030	0.75	Other	ML15	B	5.0	ML15
Hb 12 PA -5 ^o Envelope	45.5	Ph03	2.1	0.4	0.251	0.028	0.75	Other	ML15	B	5.0	ML15
He 2-111	196.9	PM89			1.000		5.0	Other	We88	B	74.0	Lo93
He 2-114	135.0	KJ89			> 1.000		5.0	Other	We88	B	25.0	We88
He 3-1357	45.6	Ot17	1.5		0.094		4.5	Whole	GH02	B	1.4	GH02
Hf 48 Hen 2-60	219.4	PM91			> 1.000		5.0	Other	We88	B	21.0	We88
Hu 1-2	111.0	Ph03			0.039		1.2	Centre	Lu01	B	11.0	Fa15
IC 418 Centre	44.5	Ph03			< 0.042		5.0	Other	St84	E	15.0	RL12
IC 2003	99.8	Ph03			< 0.030		5.0	Other	Ge91	R	8.6	Fe97
IC 2003 Center	99.8	Ph03			0.034	0.040	1.0	Other	Ho99	R	8.6	Fe97
IC 2003	99.8	Ph03			0.053	0.031	1.8	Centre	Li06	R	8.6	Fe97
IC 2165	190.0	Ph03	> 1.0		0.020		5.0	Other	Ge91	R	8.0	Mi18
IC 2165	190.0	Ph03			< 0.030		1.8	Centre	Li06	R	8.0	Mi18
IC 4406 Centre	96.8	Ph03			1.351		5.0	Other	St84	B	30.0	St84
IC 4997	62.0	Ph03			< 0.200		10.0	Whole	Be78	B	2.2	ML15
IC 4997	62.0	Ph03	> 3.0		0.012	0.005	5.0	Whole	Ge91	B	2.2	ML15
IC 5117	82.6	Ph03			0.120	0.060	12.0	Whole	Is84	M	1.1	Hs14
IC 5117	82.6	Ph03	3.7	1.3	0.110	0.011	5.0	Whole	Ge91	M	1.1	Hs14
IC 5117	82.6	Ph03			0.093	0.009	3.0	Whole	Ru01	M	1.1	Hs14
IC 5117	82.6	Ph03	6.0	1.1	0.097	0.044	1.8	Whole	Li06	M	1.1	Hs14
IC 5217	78.2	Ph03			< 0.008		1.8	Other	Li06	B	6.6	Hy01
J900	106.0	Ph03			0.210	0.060	12.0	Whole	Is84	R	10.0	Sh95
J900	106.0	Ph03			0.148	0.022	1.8	Centre	Li06	R	10.0	Sh95
K 3-60	185.0	Lu01			0.128		1.2	Whole	Lu01	I	1.0	St16
K 3-67	59.2	Lu01			0.019		1.2	Centre	Lu01	B	2.5	Sa11
K 4-48	125.0	Lu01	8.9		0.523		1.2	Other	Lu01	?	2.2	St08
LMC SMP-06	140	Ma16			0.098	0.006	0.75	Whole	Ma16	E	0.67	Sh06
LMC SMP-47	150	Ma16	9.4	0.8	0.321	0.009	0.75	Whole	Ma16	E	0.45	Sh06
LMC SMP-62	100	Ma16	> 2.9		0.014	0.002	0.45	Other	Ma16	E	0.59	Sh06
LMC SMP-73	135	Ma16	22.5	6.1	0.275	0.037	0.75	Whole	Ma16	E	0.31	Sh06
LMC SMP-85	46	Ma16	1.7	0.4	0.033	0.005	0.75	Whole	Ma16	U	<0.163	HB04
LMC SMP-99	124	Ma16			0.037	0.010	0.75	Other	Ma16	B	0.82	St07
M 1-4	40.3	Ph03			< 0.02		1.8	Centre	Li06	R	7.4	Sa11
M 1-6	34.5	Ph03			< 0.07		1.8	Centre	Li06	B	3.4	Sa11
M 1-11	32.0	Ot13	2.7		0.058		1.2	Centre	Lu01	R	2.0	Ot13
M 1-11	32.0	Ot13	2.5	0.2	0.085	0.006	1.0	Centre	Ot13	R	2.0	Ot13
M 1-13	118.1	PM91	7.7	2.5	1.667	0.767	1.8	Other	Li06	B	12.0	Li06
M 1-74	58.0	Ph03	2.8		0.061		1.2	Whole	Lu01	U	1.0	SS99

Table A1. (Cont) Observations Database

Object	T^* (10^3 K)	T^* Ref.	$R(H_2)$	$R(H_2)$ Error	$R(Bry)$	$R(Bry)$ Error	w (arcsec)	Slit Position	H_2 Ref.	Morph.	D (arcsec)	D Ref.
M 1-75 Lobes	200.0	Hu88	12.4	3.7	8.300	2.033	0.75	H_2 Peak	ML15	M	18.0	Gu00
M 1-75 Ring	200.0	Hu88	12.3	2.8	1.760	0.179	0.75	H_2 Peak	ML15	M	18.0	Gu00
M 1-75 Centre	200.0	Hu88			0.477	0.037	0.75	Other	ML15	M	18.0	Gu00
M 2-9	43.3	Ph03	> 3.9		0.254		8.0	Centre	Ph85	B	10.0	HL94
M 2-9 Core	43.3	Ph03			< 0.001		0.8	Other	HL94	B	10.0	HL94
M 2-9 N knot	43.3	Ph03	5.0		0.150		0.8	Other	HL94	B	10.0	HL94
M 2-9 Lobe I	43.3	Ph03	9.1		3.030		0.8	H_2 Peak	HL94	B	10.0	HL94
M 2-9 Lobe M	43.3	Ph03	10.3		5.882		0.8	H_2 Peak	HL94	B	10.0	HL94
M 2-9 Lobe O	43.3	Ph03	9.1		19.61		0.8	H_2 Peak	HL94	B	10.0	HL94
M 4-17 PA 130 $^\circ$ All	127.0	St02	6.5	1.0	3.070	0.436	0.75	Other	ML15	B	24.0	Gu00
M 4-17 PA 40 $^\circ$ Ring	127.0	St02	8.7	2.0	5.300	0.986	0.75	H_2 Peak	ML15	B	24.0	Gu00
M 4-17 PA 40 $^\circ$ Centre	127.0	St02	7.7	0.6	2.100	0.123	0.75	Other	ML15	B	24.0	Gu00
Me 2-1	180.0	Ph03			< 0.170		5.0	Centre	St84	R	8.7	Su04
Me 2-1	180.0	Ph03			< 0.050		1.8	Centre	Li06	R	8.7	Su04
MyCn 18	51.6	Ph03			< 0.200		5.0	Other	We88	B	6.0	C114
Mz 1	139.0	KJ89			> 1.000		5.0	Other	We88	B	58.4	Ma98
NGC 40 W Lobe	33.8	Ph03	6.1	4.7	0.069	0.018	1.0	Other	He99	B	45.0	LF11
NGC 40 W	33.8	Ph03	> 2.4		0.058	0.030	1.8	Other	Li06	B	45.0	LF11
NGC 40 E	33.8	Ph03			< 0.040		1.8	Other	Li06	B	45.0	LF11
NGC 1535 Centre	76.3	Ph03			< 0.450		5.0	Other	St84	R	35.0	BA91
NGC 2346	100.0	Ma15			5.000		5.0	Other	We88	B	47.0	Vi99
NGC 2346 W filament	100.0	Ma15	12.2	4.4	25.875	16.253	1.0	H_2 Peak	He99	B	47.0	Vi99
NGC 2346 W	100.0	Ma15	14.3		11.494		3.5	H_2 Peak	Vi99	B	47.0	Vi99
NGC 2346 E	100.0	Ma15	14.9		21.277		3.5	H_2 Peak	Vi99	B	47.0	Vi99
NGC 2346 S	100.0	Ma15	> 11.1		> 6.250		3.5	Other	Vi99	B	47.0	Vi99
NGC 2440	200.0	HH90			0.160	0.040	12.0	Other	Is84	B	80.0	CP00
NGC 2440	200.0	HH90	> 13.5		0.270	0.022	5.0	Other	Ge91	B	80.0	CP00
NGC 2440 NE Clump	200.0	HH90	11.7	8.5	8.200	4.220	1.0	H_2 Peak	He99	B	80.0	CP00
NGC 2440 N Lobe	200.0	HH90	8.4	6.2	0.207	0.039	1.0	Other	He99	B	80.0	CP00
NGC 2440 E Lobe	200.0	HH90			0.627	0.205	1.0	Other	He99	B	80.0	CP00
NGC 2792 Centre	114.2	Ph03			< 0.130		5.0	Centre	St84	R	10.0	Po99
NGC 2818 20 $^\circ$ S	215.0	Ph03			> 3.420		5.0	Other	St84	B	57.1	Va12
NGC 2818 30 $^\circ$ E	215.0	Ph03			> 3.540		5.0	Other	St84	B	57.1	Va12
NGC 2818	215.0	Ph03			> 35.000		5.0	Other	We88	B	57.1	Va12
NGC 2899	270.0	Fr08			3.000		5.0	Other	We88	B	60.0	Lo01
NGC 3132 Centre	80.1	Ph03			> 3.820		5.0	Other	St84	R	90.0	Mo00
NGC 3132 20 $^\circ$ N	80.1	Ph03			> 4.290		5.0	H_2 Peak	St84	R	90.0	Mo00
NGC 3132 20 $^\circ$ E	80.1	Ph03	10.0		> 10.480		5.0	H_2 Peak	St84	R	90.0	Mo00
NGC 3132	80.1	Ph03			10.50		5.0	Other	We88	R	90.0	Mo00
NGC 3242 Centre	89.9	Ph03			< 0.080		5.0	Other	St84	R	20.0	BK18
NGC 3242 15 $^\circ$ E	89.9	Ph03			< 0.170		5.0	Other	St84	R	20.0	BK18
NGC 3242	89.9	Ph03			< 0.007		5.0	Other	Ge91	R	20.0	BK18
NGC 4071	118.0	Ph03			> 1.000		5.0	Other	We88	B	66.7	Be17
NGC 5189	109.8	Ph03			> 1.000		5.0	Other	We88	P	210.0	Be17
NGC 6072 Centre	147.0	Ph03			> 4.210		5.0	Other	St84	M	67.0	Kw10
NGC 6072 20 $^\circ$ E	147.0	Ph03			> 5.710		5.0	Other	St84	M	67.0	Kw10
NGC 6072 20 $^\circ$ W	147.0	Ph03			> 6.180		5.0	Other	St84	M	67.0	Kw10
NGC 6153 Centre	97.1	Ph03			< 0.110		5.0	Other	St84	B	17.0	Yu11
NGC 6153 10 $^\circ$ E	97.1	Ph03			< 0.050		5.0	H_2 Peak	St84	B	17.0	Yu11
NGC 6153 10 $^\circ$ W	97.1	Ph03			< 0.080		5.0	H_2 Peak	St84	B	17.0	Yu11
NGC 6210	61.1	Ph03			0.050	0.020	5.0	Other	Is84	I	15.0	Po09b
NGC 6210	61.1	Ph03			< 0.010		5.0	Other	Ge91	I	15.0	Po09b
NGC 6210	61.1	Ph03			< 0.007		1.8	Other	Li06	I	15.0	Po09b
NGC 6302	200.0	Sz09			0.084		7.5	Other	Ph83	B	97.0	Sz11
NGC 6302	200.0	Sz09	> 3.0		0.090	0.030	5.0	Other	Ge91	B	97.0	Sz11
NGC 6302 up2	200.0	Sz09	3.5	0.9	1.300	0.200	2.0	Other	Da03	B	97.0	Sz11
NGC 6302 up	200.0	Sz09	3.2	0.7	0.160	0.040	2.0	Other	Da03	B	97.0	Sz11
NGC 6302 cen	200.0	Sz09	6.7	1.4	0.100	0.010	2.0	Other	Da03	B	97.0	Sz11
NGC 6302 dn	200.0	Sz09	3.9	0.6	0.140	0.010	2.0	Other	Da03	B	97.0	Sz11
NGC 6302 dn2	200.0	Sz09	2.1	0.8	0.600	0.100	2.0	Other	Da03	B	97.0	Sz11
NGC 6302 dn3	200.0	Sz09	12.6	2.0	3.900	0.400	2.0	Other	Da03	B	97.0	Sz11

Table A1. (Cont) Observations Database

Object	T★ (10 ³ K)	T★ Ref.	R(H ₂)	R(H ₂) Error	R(Bry)	R(Bry) Error	w (arcsec)	Slit Position	H ₂ Ref.	Morph.	D (arcsec)	D Ref.
NGC 6445 up	182.7	Ph03	10.2	2.0	2.000	0.100	2.0	H ₂ Peak	Da03	B	42.0	Da03
NGC 6445 cen	182.7	Ph03	8.3	3.0	1.200	0.100	2.0	H ₂ Peak	Da03	B	42.0	Da03
NGC 6445 dn	182.7	Ph03			0.370	0.020	2.0	H ₂ Peak	Da03	B	42.0	Da03
NGC 6445 dn2	182.7	Ph03	9.8	1.0	1.400	0.100	2.0	H ₂ Peak	Da03	B	42.0	Da03
NGC 6537	250.0	KJ89	> 3.8		0.060	0.010	5.0	Other	Ge91	B	50.0	Da03
NGC 6537 up	250.0	KJ89	4.2	1.8	0.140	0.010	2.0	Other	Da03	B	50.0	Da03
NGC 6537 cen	250.0	KJ89	8.4	2.5	0.100	0.010	2.0	Other	Da03	B	50.0	Da03
NGC 6537 dn	250.0	KJ89	4.0	1.8	0.130	0.010	2.0	Other	Da03	B	50.0	Da03
NGC 6572	66.8	Ph03			< 0.025		10.0	Centre	Be78	B	7.0	Mi99
NGC 6572	66.8	Ph03			< 0.004		5.0	Other	Ge91	B	7.0	Mi99
NGC 6720	120.6	Ph03			3.238	0.500	10.0	H ₂ Peak	Be78	R	88.0	OD03
NGC 6720 L	120.6	Ph03	9.0	2.3	3.303	0.362	1.0	H ₂ Peak	Ho99	R	88.0	OD03
NGC 6772	119.9	Ph03			> 1.000		5.0	Other	We88	R	90.0	Fa18
NGC 6778	96.9	Ph03			< 1.000		5.0	Other	We88	B	20.0	GM12
NGC 6790	74.0	Ph03			< 0.170		10.0	Whole	Be78	R	1.8	ZK91
NGC 6881 PA 137 ^o	95.6	Ph03	7.5		0.109		0.75	Other	RL08	B	9.0	RL08
Central												
NGC 6881 PA 137 ^o	95.6	Ph03			4.308		0.75	Other	RL08	B	9.0	RL08
H ₂ Lobes												
NGC 6881 PA 137 ^o	95.6	Ph03			0.855		0.75	Other	RL08	B	9.0	RL08
Ion. Lobes												
NGC 6881 PA 113 ^o	95.6	Ph03	6.5		12.222		0.75	H ₂ Peak	RL08	B	9.0	RL08
H ₂ Lobes												
NGC 6881 PA 113 ^o	95.6	Ph03	5.7		0.919		0.75	Other	RL08	B	9.0	RL08
Ion. Lobes												
NGC 6886 up	129.0	Ph03	6.1	0.6	0.170	0.010	2.0	H ₂ Peak	Da03	B	6.0	Da03
NGC 6886 cen	129.0	Ph03	10.5	2.0	0.110	0.010	2.0	Other	Da03	B	6.0	Da03
NGC 6886 dn	129.0	Ph03	5.8	0.5	0.170	0.010	2.0	H ₂ Peak	Da03	B	6.0	Da03
NGC 7009	87.8	Ph03			< 1.000		5.0	Other	We88	B	50.0	Wa18
NGC 7027	198.0	La00	> 4.1		0.070	0.022	7.0	Other	Sm81	M	7.3	La16
NGC 7027	198.0	La00	22.4	9.2	0.056	0.006	5.0	Other	Ge91	M	7.3	La16
NGC 7027 NW	198.0	La00	13.2	7.2	0.357	0.025	1.0	H ₂ Peak	Ho99	M	7.3	La16
H ₂ Lobe												
NGC 7027 W Lobe	198.0	La00			0.051	0.014	1.0	Other	Ho99	M	7.3	La16
NGC 7027	198.0	La00			0.096		1.2	Other	Lu01	M	7.3	La16
NGC 7048 up2	119.5	Ph03	19.2	2.4	15.000	6.000	2.0	H ₂ Peak	Da03	B	60.0	Da03
NGC 7048 up	119.5	Ph03	12.7	2.0	13.000	3.000	2.0	H ₂ Peak	Da03	B	60.0	Da03
NGC 7048 cen	119.5	Ph03	12.3	1.8	10.000	1.800	2.0	H ₂ Peak	Da03	B	60.0	Da03
NGC 7048 dn	119.5	Ph03	20.0	2.5	18.000	3.000	2.0	H ₂ Peak	Da03	B	60.0	Da03
NGC 7048 dn2	119.5	Ph03	10.4	1.9	8.700	1.800	2.0	H ₂ Peak	Da03	B	60.0	Da03
NGC 7048 dn3	119.5	Ph03	14.5	0.8	26.000	2.000	2.0	H ₂ Peak	Da03	B	60.0	Da03
NGC 7293 5 'N	108.5	Ph03			> 2.190		5.0	H ₂ Peak	St84	R	1300.0	He99
NGC 7293 7 'E	108.5	Ph03			> 1.470		5.0	H ₂ Peak	St84	R	1300.0	He99
NGC 7293 7 'W	108.5	Ph03			> 4.470		5.0	H ₂ Peak	St84	R	1300.0	He99
NGC 7662	109.9	Ph03			0.130		5.0	Other	Is84	R	35.0	BK18
NGC 7662	109.9	Ph03	> 1.0		< 0.020		5.0	Other	Ge91	R	35.0	BK18
SwSt 1	35.5	Ph03			0.042		0.6	Centre	DM01	R	1.3	DM01
SwSt 1	35.5	Ph03	> 8.0		0.057	0.028	1.8	Whole	Li06	R	1.3	DM01
Vy 1-2	99.8	Ph03			< 0.030		1.8	Other	Li06	B	3.0	Ak15
Vy 2-2 Core	59.5	Ph03			0.035	0.010	1.0	Whole	Ho99	U	0.5	CS98
Vy 2-2	59.5	Ph03	> 7.0		0.032	0.017	1.8	Whole	Li06	U	0.5	CS98